

An HST search for planets in the lower Main Sequence of the globular cluster NGC 6397[★]

V. Nascimbeni^{1,2,3★★}, L. R. Bedin^{2,3}, G. Piotto^{1,2}, F. De Marchi⁴, and R. M. Rich⁵

¹ Dipartimento di Astronomia, Università degli Studi di Padova, Vicolo dell'Osservatorio 3, 35122 Padova, Italy
e-mail: valerio.nascimbeni@unipd.it, giampaolo.piotto@unipd.it

² INAF – Osservatorio Astronomico di Padova, vicolo dell'Osservatorio 5, 35122 Padova, Italy
e-mail: luigi.bedin@oapd.inaf.it

³ Space Telescope Science Institute, 3700 San Martin Drive, Baltimore, MD 21218

⁴ Dipartimento di Fisica, Università di Roma Tor Vergata and INFN, Sezione di Roma Tor Vergata, I-00133 Roma
e-mail: fabrizio.demarchi@roma2.infn.it

⁵ Division of Astronomy and Astrophysics, University of California, Los Angeles, 430 Portola Plaza, Box 951547, Los Angeles, CA 90095-1547, USA. e-mail: rmr@astro.ucla.edu

Submitted December 16, 2011; accepted February 16, 2012

ABSTRACT

Searches for planetary transits carried out in open and globular clusters have yielded to date only a handful of weak, unconfirmed candidates. These results have been interpreted either as being insignificant, or as evidence that the cluster chemical or dynamical environment inhibits the planetary formation or survival. Most campaigns were limited by small sample statistics or systematics from ground-based photometry. In this work we performed a search for transiting planets and variables in a deep stellar field of NGC 6397 imaged by HST-ACS for 126 orbits. We analyzed 5,078 light curves, including a pure sample of 2,215 cluster-member M0–M9 dwarfs. The light curves have been corrected for systematic trends and inspected with several tools. No high-significance planetary candidate is detected. We compared this null detection with the most recent results from Kepler, showing that no conclusive evidence of lower planet incidence can be drawn. However, a very small photometric jitter is measured for early-M cluster members ($\lesssim 2$ mmag on 98% of them), which may be worth targeting in the near future with more optimized campaigns. Twelve variable stars are reported for the first time.

Key words. techniques: photometric – stars: planetary systems – clusters: individual: NGC 6397

1. Introduction

More than seven-hundred extrasolar planets are known (exo-planet.eu database). Most of them are characterized only by means of radial velocities (RV) and lack any information about their “real” mass M_p , because it can be measured only $M_p \sin i$, being i the inclination of the orbit with respect to the line of sight. Their size is also unknown, which prevents us from getting any clues about their density and physical composition. Exoplanetary transits are highly complementary to RV techniques, providing the planetary radius R_p from the stellar radius R_\star in a direct geometrical way (Seager 2011, p. 55). Photometric searches for transits can also go much deeper than RVs in magnitude, and can monitor thousands of stars simultaneously. The Kepler mission (Borucki et al. 2010), for instance, is demonstrating the power of this technique by discovering many planetary systems with unexpected properties. Hundreds of Kepler “candidate planets”, for which confirmation and mass measurement via RVs remains infeasible, are still very useful for statistical purposes (Howard et al. 2011; Schlaufman & Laughlin 2011).

Star clusters, and in particular globular clusters (GC), offer a unique opportunity to study how the chemical and dy-

namical environment affects the planetary formation and evolution. They are also comprised of stars that share (in most cases) the same age and chemistry, and whose radii R_\star and masses M_\star are reliably known on their main sequence (MS). Open clusters (OC) have been targeted for extensive transit searches (Mochejska et al. 2005; Montalto et al. 2007, 2011; Hartman et al. 2009, most notably) but only a handful of weak, unconfirmed candidates have been detected so far (Mochejska et al. 2006; Montalto et al. 2011). A global reanalysis suggests that the overall statistical significance of these campaigns is so low that it could be compatible with the planet host incidence observed in the field (van Saders & Gaudi 2011). GCs, on the other hand, are on average much richer in stars than OCs, providing more statistical significance in case of null detection. The only GCs monitored for transits have been 47 Tucanae for eight days with HST WFPC2 (Gilliland et al. 2000) and for 33 days from the ground (Weldrake et al. 2005); and ω Centauri with a 25-day ground-based campaign (Weldrake et al. 2008). No planetary detection has been claimed, and Gilliland et al. (2000) concluded that the planet occurrence in 47 Tuc is smaller by a factor of ten compared to field stars. The reasons which have been mostly hypothesized to explain the lack of giant planets in GCs are their metallicity, and their dynamical environment.

It has long been known that metallicity is a strong primary parameter that correlates with the fraction of stars with planets Φ_p . For giant planets Fischer & Valenti (2005), among others, showed an increase from the typical value $\Phi_p^\odot \sim 0.03$ for

[★] Based on observations with the NASA/ESA Hubble Space Telescope, obtained at the Space Telescope Science Institute, which is operated by AURA, Inc., under NASA contract NAS 5-26555.

^{★★} Visiting PhD Student at STScI (DDRF D0001.82432 program).

stars with solar metallicity up to $\Phi_p \sim 0.25$ for very metal-rich ($[\text{Fe}/\text{H}] \gtrsim +0.3$) stars. It is still disputed whether for moderately metal-poor stars ($-0.5 \lesssim [\text{Fe}/\text{H}] \lesssim 0$) this correlation becomes flat on values $\Phi_p \simeq \Phi_p^\odot$ (Udry & Santos 2007; Santos et al. 2011), or Φ_p continues to decrease exponentially towards lower metallicities (Johnson et al. 2010). As more and more low-mass planets ($M_p \lesssim 30M_\oplus$) are being discovered, it becomes clear that their Φ_p is much larger than that of giant planets (Lovis et al. 2009; Wittenmyer et al. 2011), probably around $\sim 20\text{--}30\%$. The occurrence of low-mass planets seems to be insensitive to the host star metallicity (Udry et al. 2006), except maybe for very late-type stars (Johnson & Apps 2009; Schlafman & Laughlin 2011), but M-dwarf metallicity calibration is still too uncertain to draw conclusions.

The complex dynamical environment of a cluster is the second major concern about the survival of protoplanetary systems. Theoretical studies give different answers, but some of them imply that gravitational stripping processes are not enough strong to disrupt very short-period ($P < 5$ days) planetary systems, even in the densest regions of a typical GC (Fregeau et al. 2006; Spurzem et al. 2009). Indeed, planets do exist in clusters. Giant planets have been detected around evolved stars belonging to open clusters (Lovis & Mayor 2007; Sato et al. 2007), and around a pulsar in the globular cluster M4 (Thorsett et al. 1999). It is therefore difficult to understand why no planets were detected in 47 Tuc. The search by Gilliland et al. (2000) was sensitive only to giant planets ($R_p \gtrsim 1R_{\text{jup}}$) around stars in the upper MS, excluding late-K and M dwarfs. More data are needed to sample other regions of the parameter space.

On the other hand, it is convenient to search for transits around KM main sequence stars because of their larger expected signal. These targets, even in the nearest GCs, are faint ($V > 18$) and extremely crowded. Space-based observations are necessary to achieve the needed signal-to-noise ratio (S/N) per time unit, and to minimize the number of false positives due to blended photometric contaminants. The wide-field imagers mounted on HST (ACS and WFC3) are unrivalled in this regard, and their large archive of deep photometric series of GCs is already available to exploit for transit searches. However, we will show in Sec. 3 that HST time-resolved photometry is influenced by many sources of systematic errors that require a careful correction. We developed specific tools to this purpose, and applied them to a test case. Other data sets (such as those on 47 Tuc) will be investigated in the near future, to test whether a more optimized campaign is worth pursuing.

In this Paper we present a search for variables and planetary transits in NGC 6397, exploiting a 126-orbit data set from the HST Advanced Camera for Surveys (ACS; GO-10424; PI:Richer). NGC 6397 is a metal-poor ($[\text{Fe}/\text{H}] \simeq -2$) core-collapsed globular cluster, and the second-closest known (Gratton et al. 2003; Richer et al. 2008). Our work is in some sense complementary to that presented by Stello & Gilliland (2009), who employed the same data set to study the microvariability of highly saturated red giants. Though these data were not optimized for a transit search, its unprecedented depth allowed us to search for planets on a homogeneous sample of 2,215 member M-dwarf stars down to the hydrogen-burning limit. M dwarfs are considered the most promising targets to discover rocky planets in the near future (Scalo et al. 2007). They are the smallest stars ($R_\star \simeq 0.1\text{--}0.5R_\odot$), and therefore the transit depth for a given planet is increased by a factor of $\sim 4\text{--}100$ compared to a solar-type host star. They are also intrinsically faint ($L_\star \simeq 0.02\text{--}5 \cdot 10^{-5}L_\odot$), meaning that an habitable planet would have an orbital period of only $P = 10\text{--}30$ days.

2. Observations and data reduction

Our analysis is based on the HST data set GO-10424 (PI: Richer), originally aimed to probe the bottom of the MS and the end of the white dwarf (WD) cooling sequence in NGC 6397 (Hansen et al. 2007; Richer et al. 2008). A single $202'' \times 202''$ field, located $5'$ from the cluster core was imaged for 126 orbits with the wide-field channel of the ACS. In each orbit a single exposure through the F606W filter was bracketed by two F814W images, with exposure times ranging between 584 and 804 s (median: 704 s). Overall, 252 F814W frames and 126 F606W frames were secured, for a total exposure time of ~ 50 hours. Shorter exposures ($t_{\text{exp}} = 1, 5, 40$ s) were also taken to measure the brightest stars, but they have not been used in our study.

The dynamic range of the “deep” exposures is perfect to our purposes, as the observed luminosity function (LF) of the cluster MS members peaks at $m_{\text{F814W}} \simeq 21$ (that is, on well-measured stars with $\text{S/N} \sim 200$ in the same filter; Fig. 1, histogram on the right panel). Saturation occurs around M0V spectral type at $m_{\text{F814W}} \simeq 18.7$ and the faintest cluster members (M9V) are found at $m_{\text{F814W}} \simeq 24$ ($\text{S/N} \sim 20$), so that a sample of $\sim 2,000$ cluster M dwarfs down to the hydrogen-burning limits is available to transit search (Fig. 1, left panel).

On the other hand, these data were not optimized to search for transit events, therefore two aspects of the observing setup are somewhat limiting. First, the time coverage of the frames is not continuous, as it is in Gilliland et al. (2000). The ~ 50 h of integration time were split among twenty-one non-contiguous days, spanning a twenty-eight day period. This translated into a much lower completeness for our search, especially for the longest periods ($P > 3$ d, see Sec. 5). The second reason is that each pointing was shifted with a ten-position dithering pattern $\Delta x, \Delta y$ plus a subpixel offset $\delta x, \delta y$. While usually dithering is a winning choice on undersampled images (Anderson & King 2000), it prevented us from reaching the best photometric accuracy possible on the brightest stars. On these targets, the amount of random noise is so low that the unavoidable flat-field and pixel-to-pixel residual errors become no more negligible. A zero-point correction, discussed in next Section, was developed to suppress these systematic errors.

We carried out the data reduction on individual bias-corrected and flat-fielded .flt images provided by the HST pipeline. We employed the master input list from Anderson et al. (2008), and the code described by Anderson & King (2006) based upon the effective PSF (ePSF) approach first developed by Anderson & King (2000). Four tests have been performed on a subset of twenty F814W frames taken at the same integer-pixel dithering position, to choose the best reduction strategy between:

1. allowing spatially-constant perturbed ePSFs as described by Anderson & King (2006);
2. correcting the raw frames for charge transfer (in)efficiency (CTE) with the pixel-based algorithm proposed by Anderson & Bedin (2010);
3. using both the 1) and 2) corrections;
4. using neither.

For all the measured sources, the RMSs of their light curve as a function of magnitude were compared. Methods 1-3 above provided no detectable improvement over the fourth choice, therefore we decided to not apply any CTE or PSF correction at this stage. In fact, actual PSFs are both spatially and temporally variable, and require a frame-to-frame *a posteriori* correction that will be explained in Section 3.

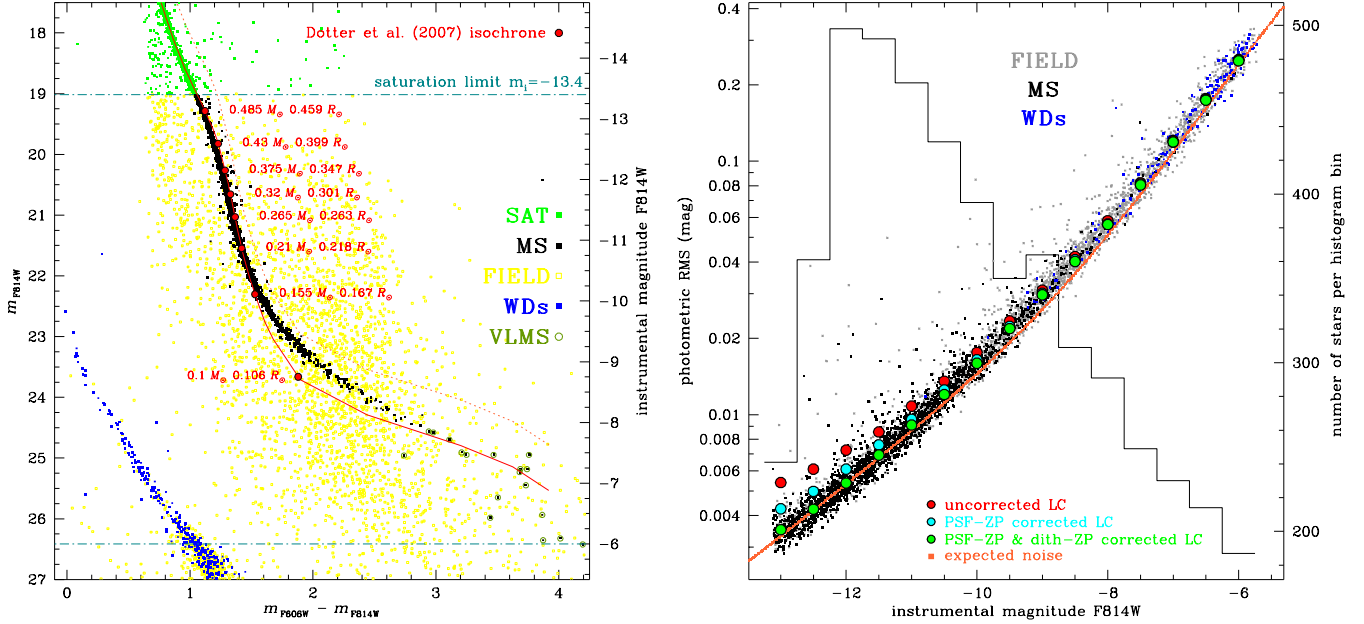


Fig. 1. *Left panel.* Color-magnitude diagram ($m_{F606W} - m_{F814W}, m_{F814W}$) for all the stars in the Anderson et al. (2008) master list; the 5,078 sources selected in this work lie between the saturation limit at $m_{F814W} \approx 19$ and the faint limit $m_{F814W} \approx 26.5$ (dash-dot lines). The red line is the isochrone by Dotter et al. (2007) employed in Richer et al. (2008). The dotted line marks the loci occupied by equal-mass MS-MS binaries. *Right panel.* RMS for light curves in our sample as a function of the instrumental magnitude. Red circles: median RMS averaged over 0.5 mag bins, without any correction. Cyan circles: the same, after PSF-ZP correction. Green circles: both PSF-ZP and dither-ZP corrections applied. Small points are the RMS of the individual light curves after both corrections. The solid orange line is the expected theoretical noise level. The superimposed histogram represents the number of targets in each 0.5 mag bin (scale at the right).

Hereafter we focus our analysis only on F814W frames for many reasons. They are much deeper than F606W images on faint, red, low MS stars, and are less affected by PSF short-term variations as showed for this very same dataset by Anderson & King (2006). The sky background is also much lower in F814W exposures. The way the F814W frames were sampled (at the beginning and the end of each 96-minute orbit) makes F606W frames nearly useless to increase the transit detection efficiency. In this way we also avoided the need to correct for tricky registration of the light curves between the two filters.

Sources beyond the saturation limit on the longest exposures ($m_{F814W} \lesssim 19$) and sources detected on less than 200 frames ($m_{F814W} \gtrsim 26.5$) have been excluded from this study, leaving 5,078 objects which include cluster members, field stars, and a limited number of non-stellar objects. We evaluated the membership of each entry by performing a selection on the proper motions between our epoch and the archival ACS GO-11633 data set (PI: Rich), centered on the same field. 2,430 sources were flagged as cluster members, of which 215 belong to the white dwarf (WD) sequence (see the CMD on Fig. 1, left panel). The remaining 2,215 MS stars are red dwarfs ranging from M0V spectral type ($R_p \approx 0.5R_{\odot}$, $M_p \approx 0.5M_{\odot}$) down to the hydrogen-burning limit, as confirmed by superimposing on the CMD an isochrone by Dotter et al. (2007), as done in Richer et al. (2008).

3. Systematic correction

The instrumental magnitude $-2.5 \log(\text{DN})$ of each star was registered to the median instrumental magnitude of stars measured on the deepest frame of the F814W series. We refer to this mag-

nitude as m . Saturation occurs at $m \lesssim -13.4$. The RMS σ_m of our full sample of 5,078 light curves has been compared with the expected noise budget, as calculated by combining theoretical photon-, dark-, background- and readout noises (right panel of Fig. 1, orange line). Individual σ_m have been averaged on 0.5 mag bins with a clipped median (red circles in the same plot) to exclude outliers from the comparison.

On average, the observed noise level on the bright side is way higher than the expected, even by 50-60% for stars with $m \lesssim -12$ (red circles, right panel of Fig. 1). We identified the source of most of this excess noise: a variation in the photometric zero point (ZP) induced by systematic changes of the PSF shape. Long-term instability of the PSF was already reported for ACS by Anderson & King (2006). We noticed that this ZP change (hereafter called *PSF-ZP*) follows a well-defined pattern as a function of time and average x, y position on the detector, measured in physical pixels. The pattern can be mapped by evaluating for each star two diagnostic parameters that appeared to be strongly correlated with the PSF-ZP shift:

1. the difference between the median magnitude $\langle m \rangle_{\text{beg}}$ measured on frames taken at the beginning of the orbit, and the median magnitude $\langle m \rangle_{\text{end}}$ from frames taken at the end of the orbit (left panel of Fig. 2, color-coded in the range -0.02 - 0.02 mag from black to red).
2. the difference between the median magnitude of the star $\langle m \rangle_{\text{7th}}$ measured on 16 consecutive frames taken during the seventh “visit” of the program ($2453451 < \text{JD} < 245352$), and the median magnitude $\langle m \rangle$ of its full light curve (right panel of Fig. 2, same scale);

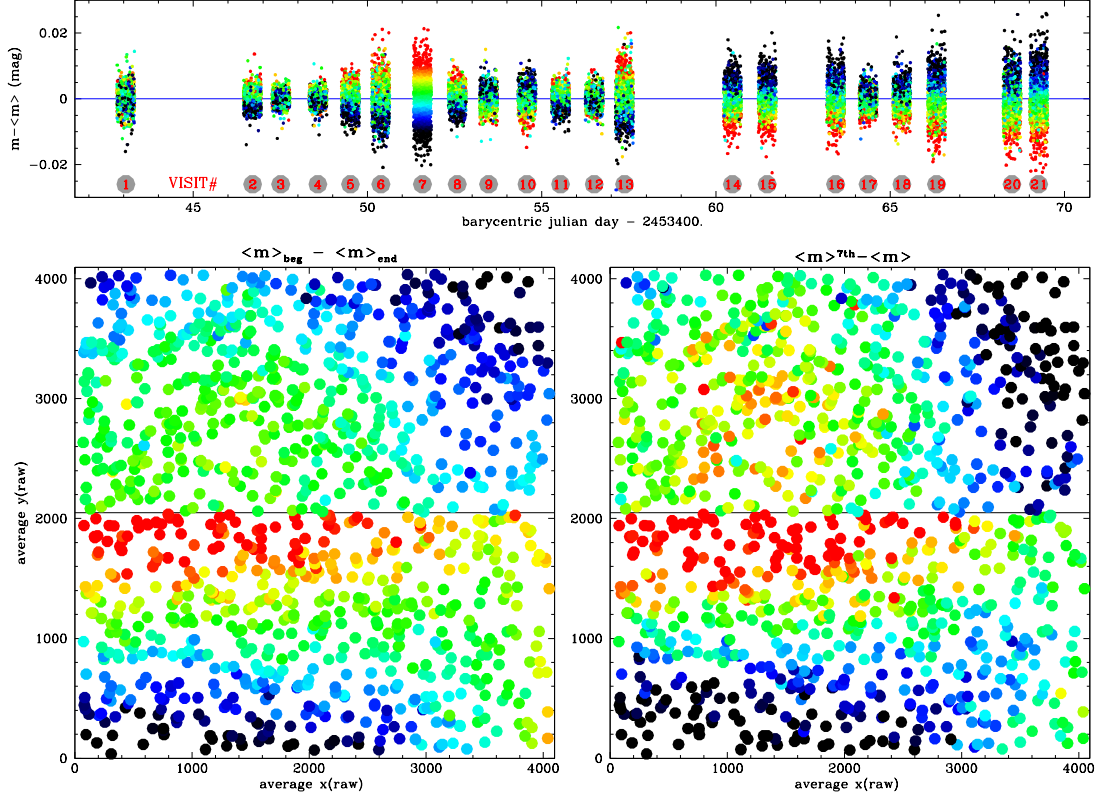


Fig. 2. Mapping the PSF-ZP shift as a function of time and position on the ACS detector, with two different diagnostics (see text). First (*left panel*) as difference between the median magnitudes $\langle m \rangle_{\text{beg}}$ and $\langle m \rangle_{\text{end}}$ measured on frames taken respectively at the beginning and at the end of the orbit. Second (*right panel*) as difference between the median magnitude of the star $\langle m \rangle^{7\text{th}}$ measured during the seventh “visit” of the program ($2453451 < \text{JD} < 245352$), and the median magnitude $\langle m \rangle$ of its full light curve. *Top panel:* All the high-S/N light curves ($\sigma_m < 0.02$) registered to their average magnitude $\langle m \rangle$. In all the panels the color scale spans the range -0.02 - 0.02 mag from black to red).

The pattern is very similar in both cases. The first diagnostic $\langle m \rangle_{\text{beg}} - \langle m \rangle_{\text{end}}$ is probably a proxy to the real origin of the PSF-ZP systematic: a thermal/mechanical instability linked to the orbital phase. The dependence of PSF-ZP on time becomes evident when all the light curves with a high S/N (i.e., measured on all the 252 frames and having $\sigma_m < 0.02$) are registered to their average magnitude $\langle m \rangle$, stacked in the same plot, and color-coded as a function of $\langle m \rangle^{7\text{th}} - \langle m \rangle$ (Fig. 2, top panel, color scale from black to red in the range -0.02 to 0.02 mag). It is clear that on average stars whose flux is overestimated during the seventh visit are also systematically underestimated in the last visits ($\text{JD} > 2453460$), and viceversa.

For a given frame, and within the same chip, the PSF-ZP is a smooth function of the position on the detector. The diagnostics $\langle m \rangle^{7\text{th}} - \langle m \rangle$ and $\langle m \rangle_{\text{beg}} - \langle m \rangle_{\text{end}}$ are too noisy when evaluated on faint stars to implement an effective correction with them. We chose instead to correct the PSF-ZP with a local approach, adapted from the differential photometry algorithms described in Nascimbeni et al. (2011). For each target star i in our sample, a set of N nearby reference stars $k = 1, \dots, N$ has been selected with the following criteria: 1) they had to lie on the same chip of the target and within 200 pixels from it, 2) they had to be at least twenty and their total flux had to exceed ten times the flux of the target, and 3) they had to be detected on at least 250 frames over 252, instead of the 200-frames limit required for a target star. When the requirement 2) was not met, the radius was in-

creased until needed. If on a given frame j a reference star k was not detected, or when its magnitude $m_{j,k}$ was more than $3\sigma_{j,k}$ off its value averaged over the series $\langle m_{j,k} \rangle$, its magnitude was set to $\langle m_{j,k} \rangle$. A reference magnitude $m_{0,j}$ was calculated on each frame by performing the weighted mean of the magnitudes of the N reference stars: $m_{0,j} = \sum_k (m_{j,k} / \sigma_{j,k}^2) / \sum_k (1 / \sigma_{j,k}^2)$ (Broeg et al. 2005). The target magnitude was then normalized to $m_{0,j}$. The PSF-ZP correction was applied only when it decreased the overall RMS of the target light curve. After the correction, the median RMS of the light curves (right panel of Fig. 1, cyan circles) is greatly improved. For the brightest stars ($m \lesssim -12$), it is decreased to a level $\sim 15\%$ above the expected noise.

Most of the remaining exceed noise is due to local ZP changes enhanced by the dithering pattern employed: an integer $\Delta x, \Delta y$ shift plus a small sub-pixel offset $\delta x, \delta y$ were added to the initial pointing x_0, y_0 (units are in physical pixels). We call this systematic effect *dith-ZP*. Each light curve, already corrected for PSF-ZP, underwent two decorrelating algorithms:

1. the median magnitude of the star $\langle m \rangle_{\Delta x, \Delta y}$ was calculated for each subset of frames sharing the same integer-pixel dither $\Delta x, \Delta y$. The magnitude m of each frame in the subset $\Delta x, \Delta y$ was then registered to $\langle m \rangle_{\Delta x, \Delta y}$.
2. for each $\Delta x, \Delta y$ subset corrected by the previous step, we considered the magnitude m_j on each frame j as a function of the sub-pixel shift $\delta x_j, \delta y_j$. A fit by ordinary linear least

squares was carried out to find the coefficients c_0, c_x, c_y such that

$$m_j = c_0 + c_x \delta x_j + c_y \delta y_j. \quad (1)$$

Once the best-fit value $m'_j = c_0 + c_x \delta x_j + c_y \delta y_j$ was evaluated for each frame, the corrected light curves were extracted and normalized to zero by evaluating $m'_j - m_j$.

Both steps 1) and 2) were applied only when the RMS decreased. The resulting median RMS of the PSF-ZP + dith-ZP correction is plotted on the right panel of Fig. 1 as green circles. The small black points on the same plot show the RMS of each single light curve of cluster members after our PSF-ZP and dith-ZP corrections have been applied. Their noise level approaches the theoretical limit on every magnitude bin, demonstrating that the algorithms we have applied have been effective.

4. Light curve analysis

4.1. Search for transit-like events

We searched for transits in the full set of 5,078 light curves (that is, including field stars) applying the box-fitting least-square algorithm (BLS, Kovács et al. 2002). For each curve BLS was set to search for periodic dips of duration Δ and depth δ with 10,000 trial periods between 0.2 and 14 days. The relative transit duration $q = \Delta/P$ was constrained to values possible for planetary transits around low-MS stars ($R_\star = 0.08\text{--}1.4R_\odot$).

For each star three detection diagnostics have been calculated: the signal residue (SR), the signal detection efficiency (SDE) associated to the maximum peak in the BLS periodogram (Kovács et al. 2002), and the detection S/N ratio defined as

$$S/N_{\text{BLS}} = \frac{\delta}{\sigma} \cdot \sqrt{n_t} \quad (2)$$

where σ is the (unbinned) photometric noise and n_t the number of data points sampled during transits.

Other more sophisticated detection diagnostics, such as the “signal-to-pink” S/N (Pont et al. 2006; Hartman et al. 2008), are robust if correlated noise σ_{red} (“red noise”, Pont et al. 2006) is present. However they require the knowledge of σ_{red} on time scales close to Δ . This is difficult to be evaluated on our data, as transits are expected to be undersampled by the observing cadence. Transits of a $P \sim 3$ d planet around a M4V star are expected to last $R_\star P/(\pi a) \sim 60$ min at most, and only $\sim 30\text{--}40$ min for later types, while images are sampled every 32 and 64 min. However, the amount of red noise here is very low, as demonstrated by the similarity of measured RMS to the theoretical one. Therefore we decided to employ both S/N_{BLS} and SDE as detection diagnostics.

To set a reliable detection criterium, 2,215 light curves were simulated, having the same sampling times t_i and noise level of the real M-dwarfs. A synthetic transit (following the analytical model by Mandel & Agol 2002) of a $1 R_{\text{jup}}$ planet was injected in each curve, with a random uniform distribution in P and $\sin i$. P was bounded to the range 1–5 d, while $\sin i$ was constrained to allow transits. The process was iterated 200 times, for a total of 450,000 injections. Then we tried to recover the transits with BLS, setting the same parameters used for the real search. A planet was defined “recovered” if at least two transits were sampled, and if the estimated orbital period (or a low-order harmonics: 2:1, 3:1, 3:2) matched the injected one. The distributions of the “injected” and “recovered” transits in the SDE vs. S/N_{BLS} plane are plotted as black and red points in the upper left panel

of Fig. 3. By dividing the parameter space in cells and evaluating the fraction of “recovered” over “injected” transits (Fig. 3, lower left panel), we obtained an estimate of the expected fraction f of real transits successfully detected (“true positives”). We defined detection criteria that guarantee a fraction of false positives smaller than 10% (that is, $f \geq 90\%$):

$$\begin{cases} \text{SDE} \geq 5.25 \\ S/N_{\text{BLS}} \geq 65 - 9 \cdot \text{SDE} \\ S/N_{\text{BLS}} \geq 7 \end{cases} \quad (3)$$

(blue line in Fig. 3). With this choice, the fraction of false negatives (that is, real planets discarded by selection criteria) is about 55%, and gets larger for planets smaller than Jupiter. This is unavoidable, if one wants to keep as low as possible the fraction of false positives.

The position of all the real sources in the (SDE, S/N_{BLS}) plane is shown in the upper-right panel of Fig. 3. Only four stars among the full sample meet the criterium set in Eq. (3) or get very close to the threshold. These “borderline” targets (ID#0269, 1961, 5936 and 7637) were inspected and cross-checked individually.

ID#269 light curve is crippled by a CCD bad pixel falling just under the star in one of the dithering positions.

ID#1961 is contaminated by brighter surrounding stars, with strong decreases of flux in one fourth of the images. The BLS signal is probably spurious.

ID#5936 seems well measured by the reduction pipeline, though it lies extremely close to a saturated star. Its light curve should be treated with caution. The parameters of the detected signal ($P \sim 2.1$ d, $\delta = 0.08$ mag, $q = 0.025$) would be compatible with a $\sim 1 R_{\text{jup}}$ transiting body with zero impact parameter, or with a grazing eclipsing binary. We classified ID#5936 as a cluster M-dwarf member analyzing its proper motion (with $M_\star = 0.34M_\odot$, $R_\star = 0.32R_\odot$ from its color), though its position in the CMD diagram is offset from the MS by 1.4 mag in m_{F814W} and 0.2 mag in color (Fig 3, lower right panel). This can not be due to binarity alone, and maybe the presence of a bright contaminant or the departure from the normal evolution of the companion play a role. There is also a non-negligible probability that ID#5936 is a field star having a proper motion compatible with the common motion of the cluster. It is worth noting that at least one data point with a similar decrease in brightness (0.08 mag, that is $\sim 4\sigma$) fell outside the expected transit windows fitted by BLS, and that the estimated duration ($\Delta = 76$ min) is way larger than the expected. We do not consider ID#5936 a convincing planetary candidate. Its coordinates are listed in Table 1 for possible further studies.

ID#7636 was rejected because it fell over a bad column on frames corresponding to “transits”.

In summary, we did not detect transits on our light curves, at least with an acceptable degree of statistical significance. We discuss the significance of this null detection in Section 5.

4.2. Search for variable stars

We performed a search for variable stars in our full database of 5,078 light curves corrected for systematic errors. First, the coefficient of spectral correlation (Ferraz-Mello 1981) was calculated for each light curve. Following the method described in de Marchi et al. (2007, 2010), we obtained a sample of thirteen suspected variable stars (Table 1). All these candidates, based on their proper motions and position in the CMD, were identified as field stars with high confidence. To classify these objects,

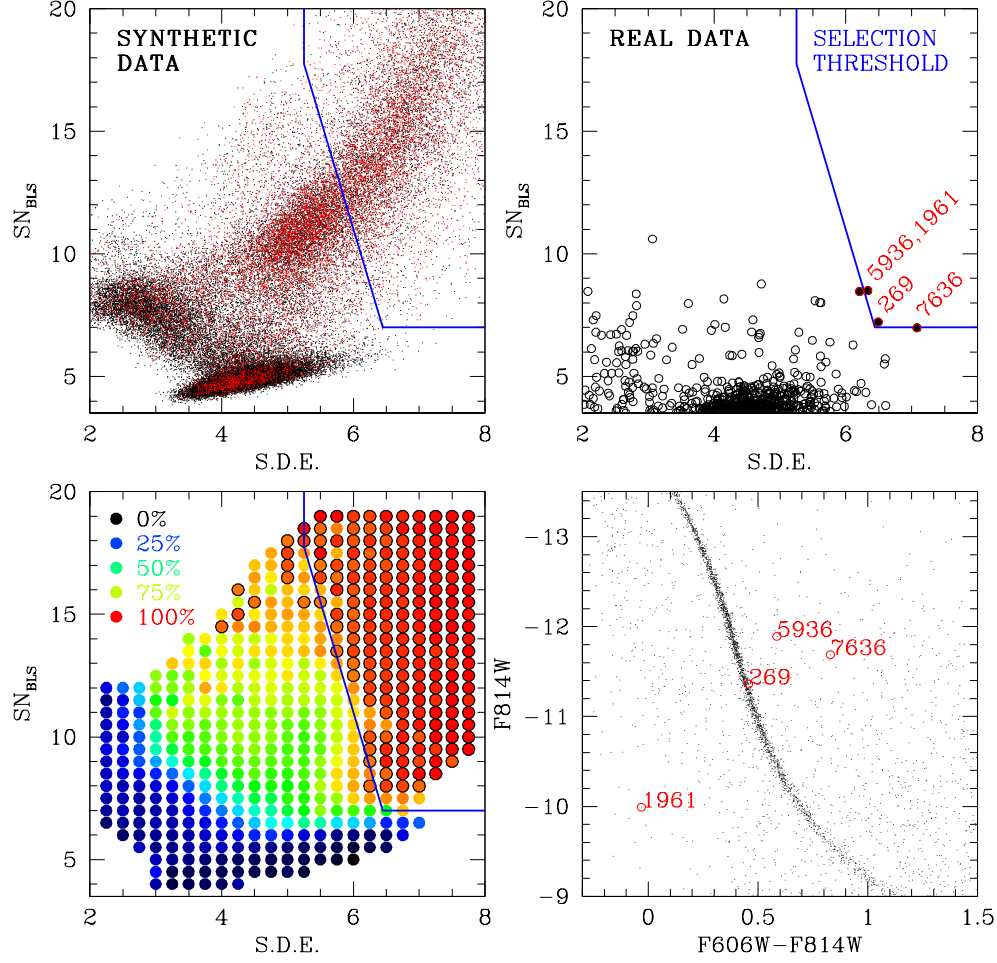


Fig. 3. *Upper left:* distribution of SDE and SN_{BLS} from the BLS analysis of 450,000 artificially injected transits on synthetic light curves. “Recovered” transits are plotted as red dots (see text). *Lower left:* same as above, where the parameter space has been divided in cells and color-coded as a function of the fraction f of transits successfully recovered. Cells with $f > 90\%$ (that is, with an incidence of false positives smaller than 10%) are highlighted with a black border. The blue line corresponds to the threshold defined in Eq. (3). *Upper right:* distribution of SDE and SN_{BLS} from the BLS analysis of the full sample of 5,078 real light curves. Four low-significance candidates are labeled. *Lower right:* location of the four low-significance candidates on the CMD.

a least-squares iterative sine-wave search was applied (Vaníček 1971).

Most of our candidates show a single harmonic sinusoidal shape, and short periods ($P \leq 9$ d): ID#830, ID#7523, ID#2178, ID#5600, ID#4957. Without other elements, it was not possible to derive an unambiguous classification for these variables. We suspect that these stars are most probably field BY Draconis variables, i.e. spotted and rotating KM dwarfs. This tentative classification is supported by their very red colors ($m_{F606W} - m_{F814W} = 1.27\text{--}2.65$).

On four stars a good best-fit can be obtained using two harmonics. The second harmonic in the light curves of ID#3428, ID#1383, ID#4430 and ID#270 could indicate the presence of spots on the surfaces and confirm the BY Dra-type classification, while in the light curve ID#6119 the second harmonic reveals the profile of a W UMa contact eclipsing binary system. Two stars (ID#2086 and ID#258) show evident orbit-to-orbit variability but time coverage is too short to infer reliable values for their periods: we classified them as generic “long period variables”.

Finally, the fluctuations in the light curve ID#1882 are too small to allow us to confirm its nature of variable star. We discarded this last candidate. The summary classification of the entire sample is reported in Table 1, along with the best candidate transit found by BLS and discussed in Section 4.1.

5. Completeness and significance

The significance of our null detection of transits was assessed by considering only the 2,215 cluster-member M dwarfs for which we derived reliable estimates of R_\star and M_\star from their position in the CMD.

For a planet of given radius R_p and orbital period P , the number of expected planet detections is given by:

$$N_p = N_\star \iint (\Phi_p(P, R_p) \cdot \Phi_{\text{geo}} \cdot \Phi_{\text{det}}) dP dR_p \quad (4)$$

where Φ_p is the fraction of stars with a planet, Φ_{geo} is the geometric *a priori* probability for that system to be aligned such

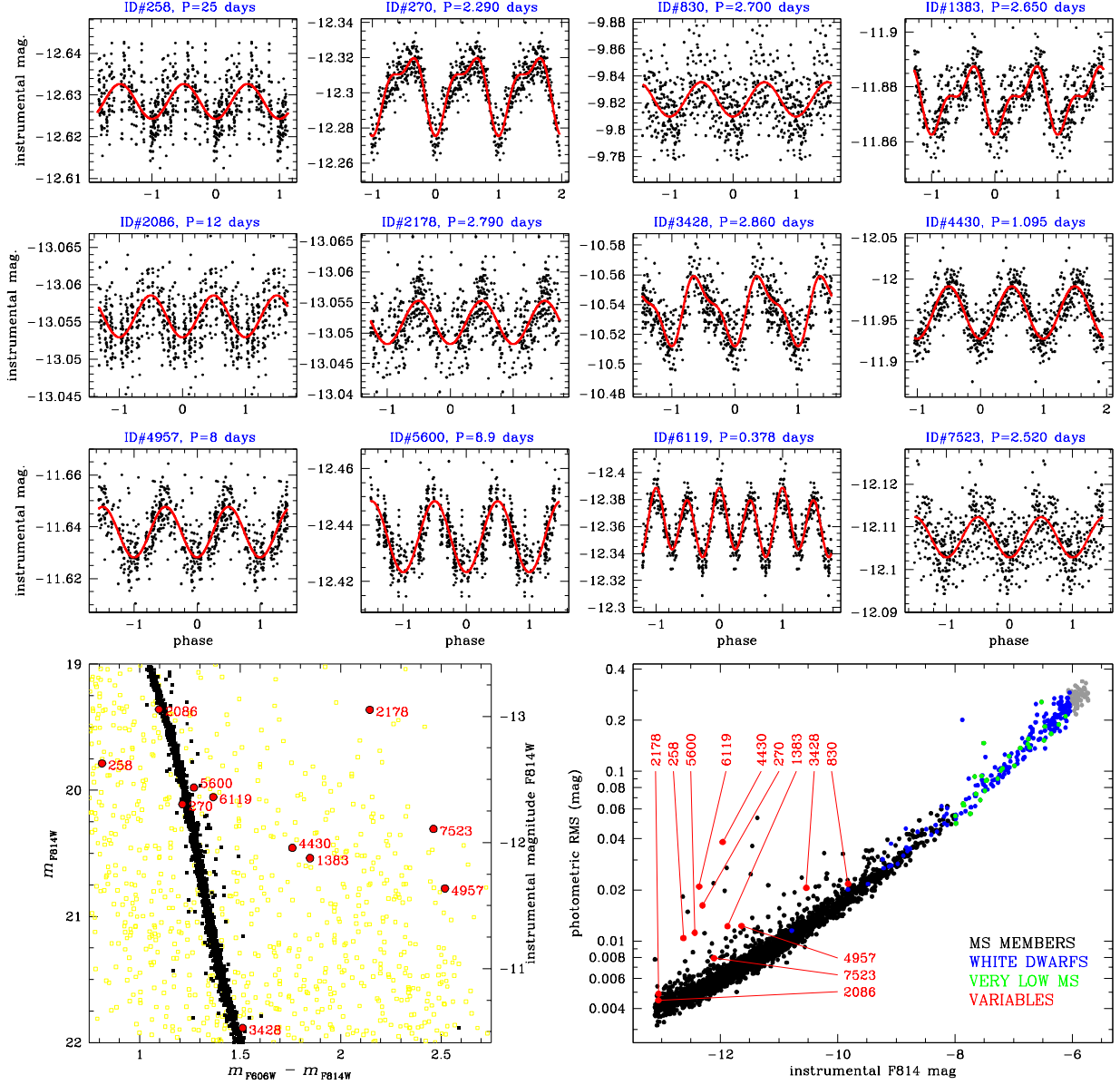


Fig. 4. *Top panels:* light curves of the variable stars found (first twelve entries in Table 1), folded around the best-fit period. *Bottom left panel:* position of the variables (red IDs) in the $(m_{F606W} - m_{F814W}, m_{F814W})$ color-magnitude diagram. *Bottom right panel:* photometric RMS of the variables (red IDs) compared with all the analyzed light curves.

that a transit occurs, Φ_{det} is the probability for that transit to be detected by our pipeline, N_* is the number of target stars. As in our case we found $N_p = 0$, we wanted to estimate an upper limit to Φ_p , at least in the (P, R_p) range for which the efficiency of our search Φ_{det} is not negligible. Φ_{det} is expected to be dependent upon the transit depth $(R_p/R_*)^2$, the duration Δ , and the orbital period P .

For simplicity, our analysis was limited to two values of planetary radii: “jupiter” planets ($1 R_{\text{jup}}$) and “neptune” planets ($0.338 R_{\text{jup}}$). To estimate Φ_{det} , we ran simulations in a way similar to what has been done to set the detection threshold (Section 4.1). In each set of 2,215 simulated light curves, a synthetic transit was injected in each curve, with a random uniform distribution in P and $\sin i$ ($1 \leq P \leq 5$ d, $\sin i$ was constrained to al-

low transits). The process was iterated 200 times, for a total of 450,000 injections. Then we tried to recover transits with BLS, setting the same parameters and detection criterium defined in Eq. (3) and adopted for the real search. To derive Φ_{det} , the ratio between detected and injected transits was evaluated for each 0.1-day bin of period P . The resulting distribution is plotted as a red line in the left panels of Fig. 5, as a function of the injected orbital period P_{in} . For comparison, the ratio between “recoverable” transits (i.e., with at least two transits sampled and $P/P_{\text{in}} = 1:1, 3:2, 2:1$) and injected transits is plotted with a green line on the same panels. As expected, Φ_{det} is a decreasing function of P , with minor features at integer and semi-integer values of P due to phasing effects. Note that for “neptunes”, Φ_{det} is extremely low (0.005–0.01) even at short periods ($P \sim 1$ –2 d).

Table 1. Parameters for the variable stars found.

ID#	RA (2000.0) h:m:s	DEC (2000.0) d:m:s	m_{F814W}	$m_{F606W} - m_{F814W}$	p.m.(α) (pixels)	p.m.(δ) (pixels)	P (days)	Δm (mag)	N_{harm}	notes
3428	17:41:06.078	-53:45:47.62	21.884	1.513	-1.2192	0.4788	2.860	0.047	2	double-wave BY Dra
1383	17:41:11.653	-53:45:02.54	20.538	1.848	-1.3037	0.2494	2.650	0.025	2	double-wave BY Dra
270	17:41:14.751	-53:45:04.94	20.110	1.213	-1.0478	0.7856	2.290	0.044	2	double-wave BY Dra
6119	17:40:58.818	-53:45:41.10	20.054	1.367	-1.4436	0.5940	0.378	0.051	2	W UMa
4430	17:41:03.155	-53:44:49.11	20.456	1.761	-1.2356	0.4401	1.095	0.069	2	BY Dra?
830	17:41:13.183	-53:45:37.72	22.598	2.654	-1.3962	0.6337	2.700	0.026	1	BY Dra?
7523	17:40:55.370	-53:45:27.03	20.306	2.463	1.0304	0.5997	2.520	0.009	1	BY Dra? (weak)
2178	17:41:09.636	-53:43:17.61	19.362	2.146	-1.6238	0.5057	2.790	0.007	1	BY Dra? (weak)
5600	17:41:00.192	-53:42:46.28	19.979	1.271	-1.5276	0.3267	≈ 8.9	0.025	1	BY Dra?
4957	17:41:01.787	-53:43:31.37	20.778	2.520	-1.6460	0.3394	≈ 8	0.019	1	BY Dra?
2086	17:41:09.888	-53:43:10.59	19.359	1.097	-1.5737	0.3106	≈ 12	0.006	1	long period
258	17:41:14.789	-53:44:58.36	19.786	0.813	-1.7434	0.3614	≈ 25	0.008	1	long period
1882	17:41:10.379	-53:44:52.05	19.430	0.792	-1.0721	0.7363	0.920	0.005	1	spurious candidate?
5936	17:40:59.316	-53:44:06.51	20.524	1.493	0.0181	0.0055	2.120	0.080	–	grazing binary?

Notes. The columns give: the ID number of the star, the right ascension α and declination δ at epoch 2000.0, the calibrated magnitude $m(F814W)$ and color $m(F814W) - m(F606W)$, the proper motion (α, δ) in ACS-WFC pixels relative to the cluster, the period found in days, the amplitude found in magnitude, the number of harmonics employed in the fit and a tentative interpretation.

This is a consequence of inefficient sampling, which makes the significance of neptunian transits very weak: 3–4 σ even for the most favourable case.

The geometric factor Φ_{geo} was calculated for each injected transit as $(R_p + R_*)/a$ (a is the semimajor axis), and then convolved with Φ_{det} to obtain the probability to detect transits on a star which is known to host a planet on a random orbit, as a function of its period (Fig. 5, middle panels).

We parametrized the “planet occurrence” following the analysis of Howard et al. (2011) on the distribution of 1,235 planetary candidates detected by Kepler. $\Phi_p(P)$ has been assumed to be a power law modified with an exponential cut-off at period P_{cut} :

$$\frac{d\Phi_p(P)}{d \log P} = k \cdot P^\beta \left(1 - e^{-(P/P_{\text{cut}})^\gamma}\right) \quad (5)$$

From Howard et al. (2011) the following parameters were adopted: $k = 0.0025$, $\beta = 0.37$, $P_{\text{cut}} = 1.7$ days, $\gamma = 4.1$ for “jupiters” ($8R_\oplus < R_p < 32R_\oplus$), and $k = 0.002$, $\beta = 0.79$, $P_{\text{cut}} = 2.2$ days, $\gamma = 4.0$ for “neptunes” ($4R_\oplus < R_p < 8R_\oplus$). $\Phi_p(P)$ is plotted, with an arbitrary normalization, as blue squares in the middle panels of Fig. 5.

We first normalized $\Phi_p(P)$ imposing $\sum_1^5 \Phi_p(P) = 1$, that is assuming one planet with $1 \text{ d} < P < 5 \text{ d}$ per star. The total number of expected detections $N_{\text{exp}}(\sum \Phi_p = 1)$ within each bin over the range $1 < P < 5 \text{ d}$ is $(\Phi_{\text{det}} \cdot \Phi_{\text{geo}} \cdot \Phi_p) N_\star$. By summing over the range $1 < P < 5 \text{ d}$, we obtained $N_{\text{exp}} = 23.8$ expected detections of “jupiters” and 0.14 of “neptunes” (right panels of Fig. 5, blue symbols). For a flat $\Phi_p(P)$ distribution, N_{exp} is larger: 42.3 and 0.45, respectively.

The upper limit $\Phi_{p,\text{max}}$ to $\sum_1^5 \Phi_p(P)$ suggested by our null detection can be evaluated by simple binomial statistics, normalizing Φ_p in order to get a 68.27% (1 σ) or 95.44% (2 σ) probability of zero detections. We estimated for jupiters $\Phi_{p,\text{max}}(1\sigma) = 4.8\%$ and $\Phi_{p,\text{max}}(2\sigma) = 12.9\%$ assuming the Howard et al. (2011) Φ_p , and $\Phi_{p,\text{max}}(1\sigma) = 3.3\%$, $\Phi_{p,\text{max}}(2\sigma) = 9.1\%$ assuming a flat Φ_p . As expected, $\Phi_{p,\text{max}}$ is well above unity for the Neptune sample, leaving this planetary population essentially unconstrained by our data (Fig. 5, lower right panel).

6. Discussion and conclusions

We performed a search for planetary transits and variability among 5,078 stars imaged in one of the deepest ACS fields ever observed, originally aimed at probing the bottom of the main sequence of the metal-poor globular cluster NGC 6397. The sample includes 2,215 M0-M9 dwarfs of proven membership. Though these data were not optimized for such a study, this is the largest homogeneous sample of M dwarfs ever searched for variability.

Instrumental drifts and systematic errors caused by dithering required a careful empirical correction, described in Section 3. We developed and implemented algorithms that allowed us to approach the theoretical noise limit on the whole magnitude range $19 \lesssim m_{F814W} \lesssim 26$. The brightest cluster members (M0V) were measured with an average scatter of 0.003–0.004 mag over a time span of 28 days, demonstrating the power of our decorrelating techniques and the feasibility of transit searches in the low main sequence of GCs.

We found no valid planetary transit above the significance threshold that we set from simulations. Considering only cluster stars, whose physical parameters can be reliably inferred, this null detection sets an upper limit to the fraction of stars hosting a $P < 5 \text{ d}$ Jupiter-sized planet to about $\Phi_p = 4.8\%$ at 1- σ confidence and 12.9% at 2- σ , assuming the planetary radius distribution derived by Howard et al. (2011) from Kepler data. In other words, only 0.13 detections are expected assuming that the underlying planetary population is similar to that studied by Kepler. Most studies based on RVs also hypothesized $\Phi_p < 1\%$ for short-period, Jupiter-sized planets around solar-type stars (Marcy et al. 2005). Furthermore, Φ_p is expected to be a very steep function of the stellar metallicity (Fischer & Valenti 2005). Therefore, we are unable to make any firm conclusion about the occurrence of giant planets in NGC 6397.

As demonstrated in Section 4.1, our data set is not enough sensitive to Neptune-sized planets to draw any conclusion about their occurrence, though a much higher Φ_p is expected for M dwarfs by Howard et al. (2011) and Lovis et al. (2009), among others. This was due to inefficient sampling of the time series available from archive material, which translated into poor phase

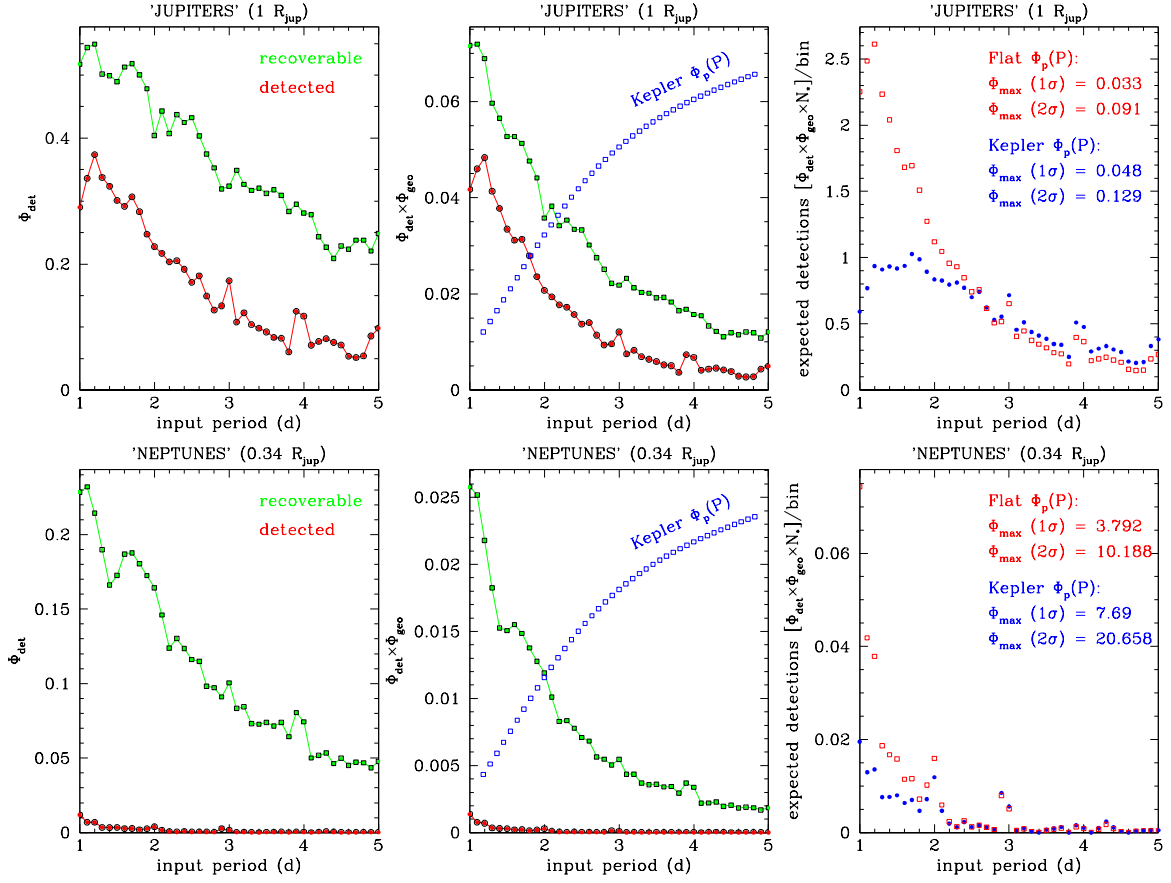


Fig. 5. Completeness tests for cluster stars based on artificially injected transits, for 1 R_{jup} planets (upper row) and 0.336 R_{jup} planets (lower row). *Left panels:* detection efficiency Φ_{det} as function of the input period, for planets potentially recoverable (green symbols) and for planets effectively detected by criterium in Eq. (3) (red symbols). *Middle panels:* same as above, but Φ_{det} is convolved with the geometrical probability Φ_{geo} for a planet to transit. The Howard et al. (2011) $\Phi_p(P)$ period distribution function is plotted in blue symbols (arbitrary normalization). *Right panels:* number of expected transit detections per period bin, assuming one planet per star within $1 < P < 5$ d. $\Phi_p(P)$ is assumed to be flat (red symbols) or as modeled by Howard et al. (2011) (blue symbols). 1- and 2- σ upper limits for the planet occurrence $\Phi_{p,\text{max}}$ are shown.

coverage and severe undersampling of transit-like events, whose duration is expected to be of the same order of the effective cadence.

Twelve new variable stars have been identified in the NGC 6397 field (Table 1). Most of them can be classified as BY Draconis variables, that is, spotted rotating KM dwarfs. Interestingly, no variable has been detected among the 2,430 cluster members. Hundreds of member early-M dwarfs ($m_{\text{F814W}} < 21$, Fig. 1) follow the expected noise on time scales up to 28 days, though they were measured with a 0.003–0.006 mag precision. The lack of eclipsing binaries is not surprising. The number of expected detections can be estimated by scaling down the number of EBs detected by Albrow et al. (2001) for 47 Tuc. If one takes into account the lower fraction of binaries in NGC 6397 ($< 3\%$, even at radii smaller than the half-mass radius, Milone et al. 2011) and the smaller number of targets (2,215 vs. 46,422), we would expect much less than one EB. On the other hand, the lack of BY Dra variables is more puzzling, as one would expect 4–5 such detections, considering the number of monitored cluster stars in this paper. We note that our stars are cooler than the Albrow et al. (2001) sample, and we should

expect longer photometric periods. Our search is not sensitive to periods ≥ 28 days, so this could be a possible explanation.

We evaluated an upper limit to the photometric jitter σ_{jit} of the brightest members (M0V) by subtracting the contribution of the expected noise σ_{exp} to the measured scatter σ_{obs} (that is, assuming $\sigma_{\text{jit}}^2 = \sigma_{\text{obs}}^2 - \sigma_{\text{exp}}^2$). The fraction of stars f with $\sigma_{\text{jit}} > 2$ mmag is $f \lesssim 2\%$. This value should be compared with the results found by Ciardi et al. (2011) examining the first quarter of Kepler photometry on 2,182 field M dwarfs: these data cover an interval of 33 days with an average cadence of 30 minutes, quite similar to our cadence and time scale. They found a fraction $f \approx 20\%$ of stars with $\sigma > 2$ mmag, that is at least an order of magnitude larger fraction than what we measured in NGC 6397. The low MS of this cluster is extremely stable and therefore worth targeting using more optimized observations. JWST NIRCcam, for instance, would be able to probe the bottom of the MS of NGC 6397 ($m_{\text{F814W}} \sim 24$) with a photometric precision better than 0.01 mag on a single 600 s exposure, without any of the coverage/sampling issues mentioned above.

Most of the analysis techniques presented in this Paper can also be applied (with little or no modification) to other exist-

ing ACS/WFC3 time series of rich stellar fields. This is the case for the metal-rich globular cluster 47 Tucanae, that has been imaged with ACS and WFC3 with a larger coverage. Such a search for transits will allow us to complement the results by Gilliland et al. (2000) in a different range of spectral types and planetary masses.

Acknowledgements. This work was partially supported by PRIN INAF 2008 "Environmental effects in the formation and evolution of extrasolar planetary system". V.N. acknowledges support by STScI grant DDRF D0001.82432. We thank Ennio Poretti for having helped us to identify the variable stars. We thank Aaron Dotter for having provided us with the isochrones used in Richer et al. (2008) and presented in Dotter et al. (2007). Some tasks of our data analysis have been carried out with the VARTOOLS code (Hartman et al. 2008). We thank Ron Gilliland for his useful comments and suggestions.

References

- Albrow, M. D., Gilliland, R. L., Brown, T. M., et al. 2001, *ApJ*, 559, 1060
 Anderson, J. & Bedin, L. R. 2010, *PASP*, 122, 1035
 Anderson, J. & King, I. R. 2000, *PASP*, 112, 1360
 Anderson, J. & King, I. R. 2006, *PSFs, Photometry, and Astronomy for the ACS/WFC*, Tech. rep.
 Anderson, J., King, I. R., Richer, H. B., et al. 2008, *AJ*, 135, 2114
 Borucki, W. J., Koch, D., Basri, G., et al. 2010, *Science*, 327, 977
 Broeg, C., Fernández, M., & Neuhäuser, R. 2005, *Astronomische Nachrichten*, 326, 134
 Ciardi, D. R., von Braun, K., Bryden, G., et al. 2011, *AJ*, 141, 108
 de Marchi, F., Poretti, E., Montalto, M., Desidera, S., & Piotto, G. 2010, *A&A*, 509, A17
 de Marchi, F., Poretti, E., Montalto, M., et al. 2007, *A&A*, 471, 515
 Dotter, A., Chaboyer, B., Jevremović, D., et al. 2007, *AJ*, 134, 376
 Ferraz-Mello, S. 1981, *AJ*, 86, 619
 Fischer, D. A. & Valenti, J. 2005, *ApJ*, 622, 1102
 Fregeau, J. M., Chatterjee, S., & Rasio, F. A. 2006, *ApJ*, 640, 1086
 Gilliland, R. L., Brown, T. M., Guhathakurta, P., et al. 2000, *ApJ*, 545, L47
 Gratton, R. G., Bragaglia, A., Carretta, E., et al. 2003, *A&A*, 408, 529
 Hansen, B. M. S., Anderson, J., Brewer, J., et al. 2007, *ApJ*, 671, 380
 Hartman, J. D., Gaudi, B. S., Holman, M. J., et al. 2008, *ApJ*, 675, 1254
 Hartman, J. D., Gaudi, B. S., Holman, M. J., et al. 2009, *ApJ*, 695, 336
 Howard, A. W., Marcy, G. W., Bryson, S. T., et al. 2011, *ArXiv e-prints*
 Johnson, J. A., Aller, K. M., Howard, A. W., & Crepp, J. R. 2010, *PASP*, 122, 905
 Johnson, J. A. & Apps, K. 2009, *ApJ*, 699, 933
 Kovács, G., Zucker, S., & Mazeh, T. 2002, *A&A*, 391, 369
 Lovis, C. & Mayor, M. 2007, *A&A*, 472, 657
 Lovis, C., Mayor, M., Bouchy, F., et al. 2009, in *IAU Symposium*, Vol. 253, IAU Symposium, 502–505
 Mandel, K. & Agol, E. 2002, *ApJ*, 580, L171
 Marcy, G., Butler, R. P., Fischer, D., et al. 2005, *Progress of Theoretical Physics Supplement*, 158, 24
 Milone, A. P., Piotto, G., Bedin, L. R., et al. 2011, *ArXiv e-prints*
 Mochejska, B. J., Stanek, K. Z., Sasselov, D. D., et al. 2006, *AJ*, 131, 1090
 Mochejska, B. J., Stanek, K. Z., Sasselov, D. D., et al. 2005, *AJ*, 129, 2856
 Montalto, M., Piotto, G., Desidera, S., et al. 2007, *A&A*, 470, 1137
 Montalto, M., Villanova, S., Koppenhoefer, J., et al. 2011, *A&A*, 535, A39
 Nascimbeni, V., Piotto, G., Bedin, L. R., & Damasso, M. 2011, *A&A*, 527, A85+
 Pont, F., Zucker, S., & Queloz, D. 2006, *MNRAS*, 373, 231
 Richer, H. B., Dotter, A., Hurley, J., et al. 2008, *AJ*, 135, 2141
 Santos, N. C., Mayor, M., Bonfils, X., et al. 2011, *A&A*, 526, A112+
 Sato, B., Izumiura, H., Toyota, E., et al. 2007, *ApJ*, 661, 527
 Scalzo, J., Kaltenegger, L., Segura, A. G., et al. 2007, *Astrobiology*, 7, 85
 Schlafman, K. C. & Laughlin, G. 2011, *ArXiv e-prints*
 Seager, S. 2011, *Exoplanets*, ed. Piper, S.
 Spurzem, R., Giersz, M., Heggge, D. C., & Lin, D. N. C. 2009, *ApJ*, 697, 458
 Stello, D. & Gilliland, R. L. 2009, *ApJ*, 700, 949
 Thorsett, S. E., Arzoumanian, Z., Camilo, F., & Lyne, A. G. 1999, *ApJ*, 523, 763
 Udry, S., Mayor, M., Benz, W., et al. 2006, *A&A*, 447, 361
 Udry, S. & Santos, N. C. 2007, *ARA&A*, 45, 397
 van Saders, J. L. & Gaudi, B. S. 2011, *ApJ*, 729, 63
 Vaníček, P. 1971, *Ap&SS*, 12, 10
 Weldrake, D. T. F., Sackett, P. D., & Bridges, T. J. 2008, *ApJ*, 674, 1117
 Weldrake, D. T. F., Sackett, P. D., Bridges, T. J., & Freeman, K. C. 2005, *ApJ*, 620, 1043
 Wittenmyer, R. A., Tinney, C. G., Butler, R. P., et al. 2011, *ArXiv e-prints*